



*Supplement of*

## **Chemical characterization of atmospheric aerosols at a high-altitude mountain site: a study of source apportionment**

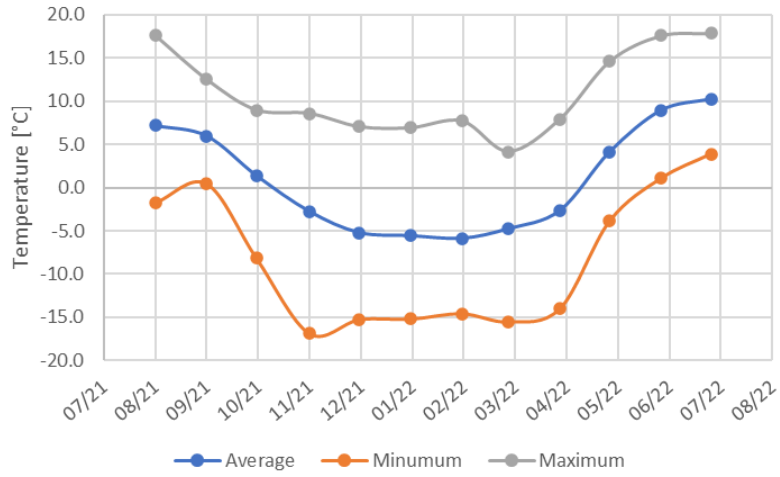
**Elena Barbaro et al.**

*Correspondence to:* Matteo Feltracco ([matteo.feltracco@unive.it](mailto:matteo.feltracco@unive.it))

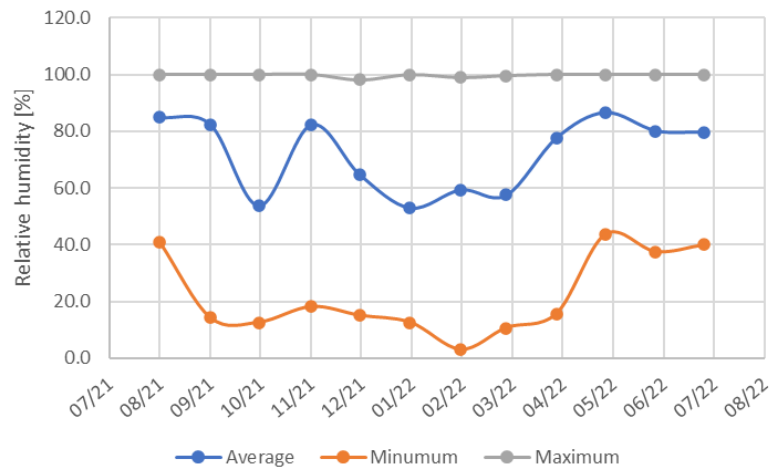
The copyright of individual parts of the supplement might differ from the article licence.

## Supplementary Materials

A)



B)



C)



Figure S1: Average and extreme values of temperature (a), relative humidity (b) and pressure (c) data during the considered period.

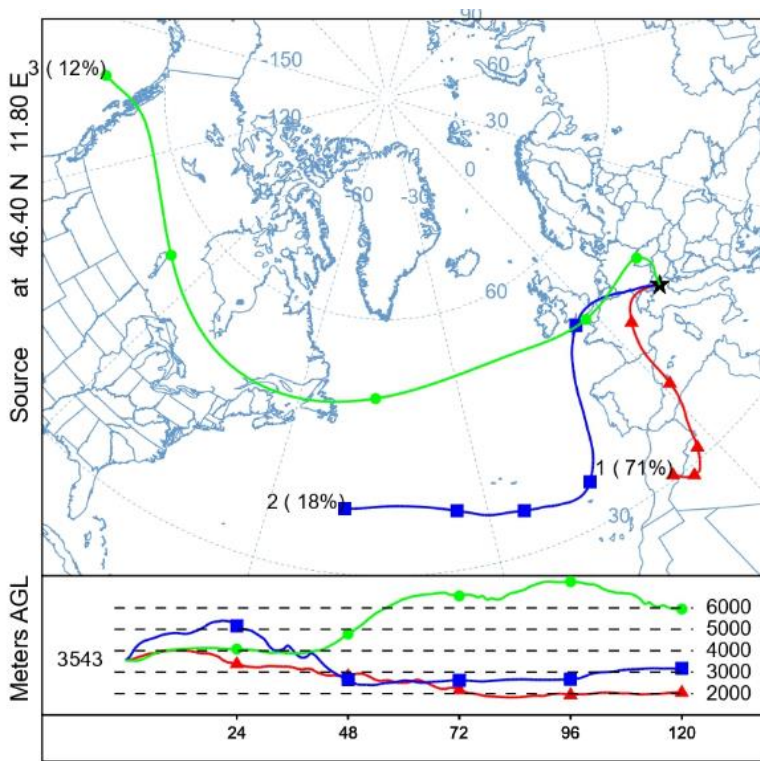


Figure S2. Cluster mean of back-trajectories during the Saharan Dust event of 15-19 March.

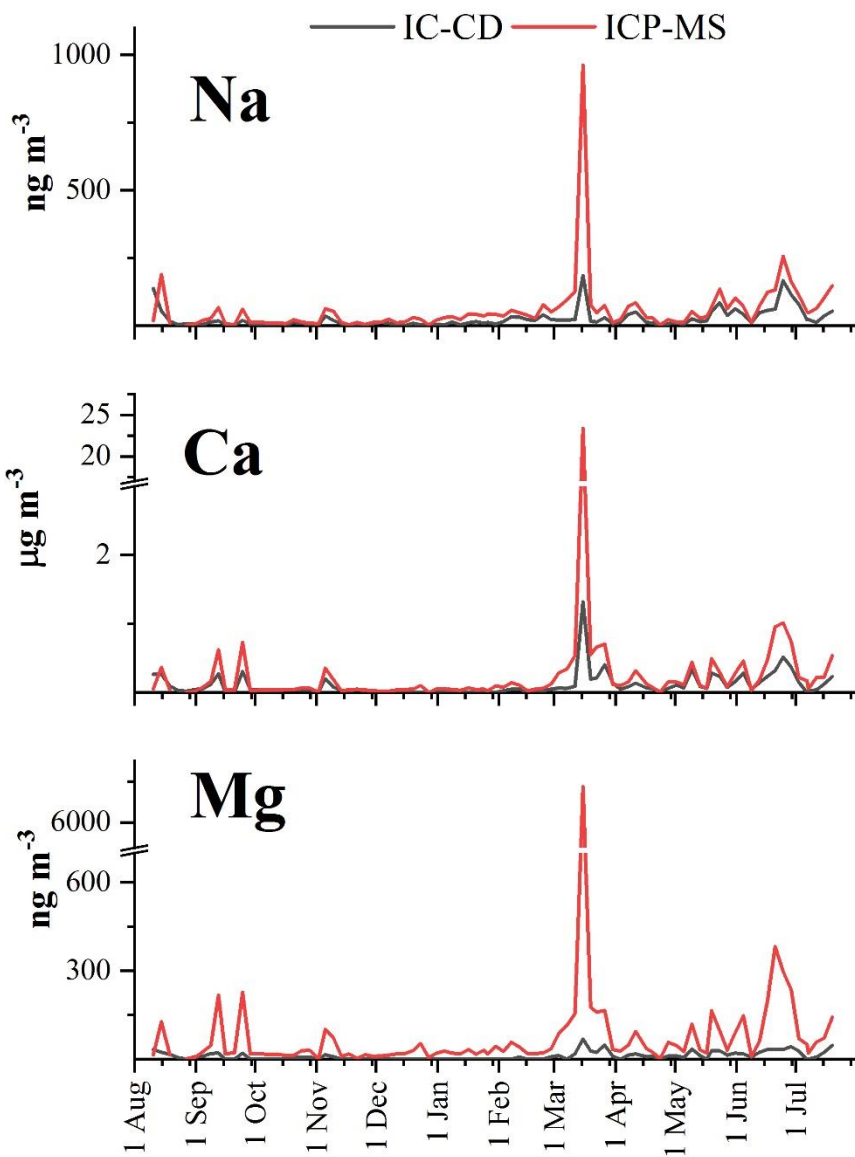
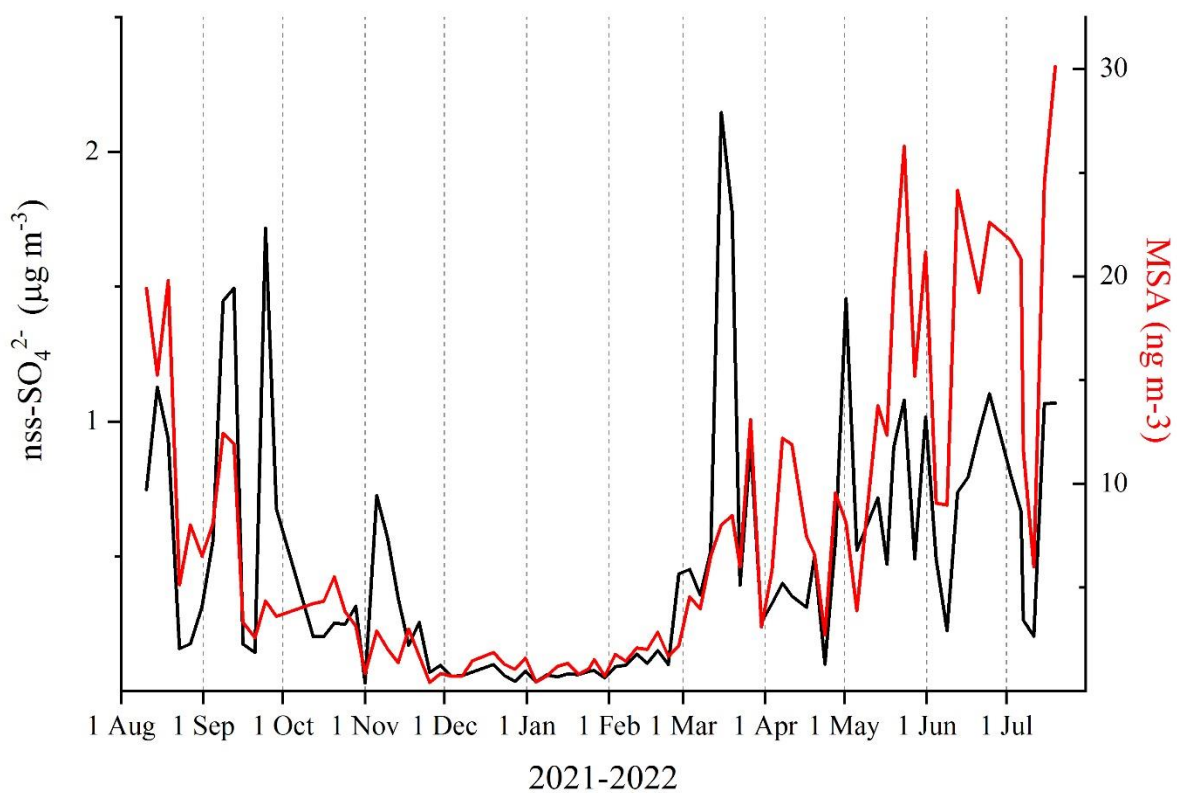


Figure S3. Comparison of sodium, calcium and magnesium concentrations performed using ion chromatography with conductivity detector (IC-CD) and inductively coupled plasma sector field mass spectrometry (ICP-SFMS).



**Figure S4.** Comparison of non-sea salt sulfate (nss-SO<sub>4</sub><sup>2-</sup>) and methansulfonic acid (MSA) during the entire sampling year at Col Margherita Observatory.

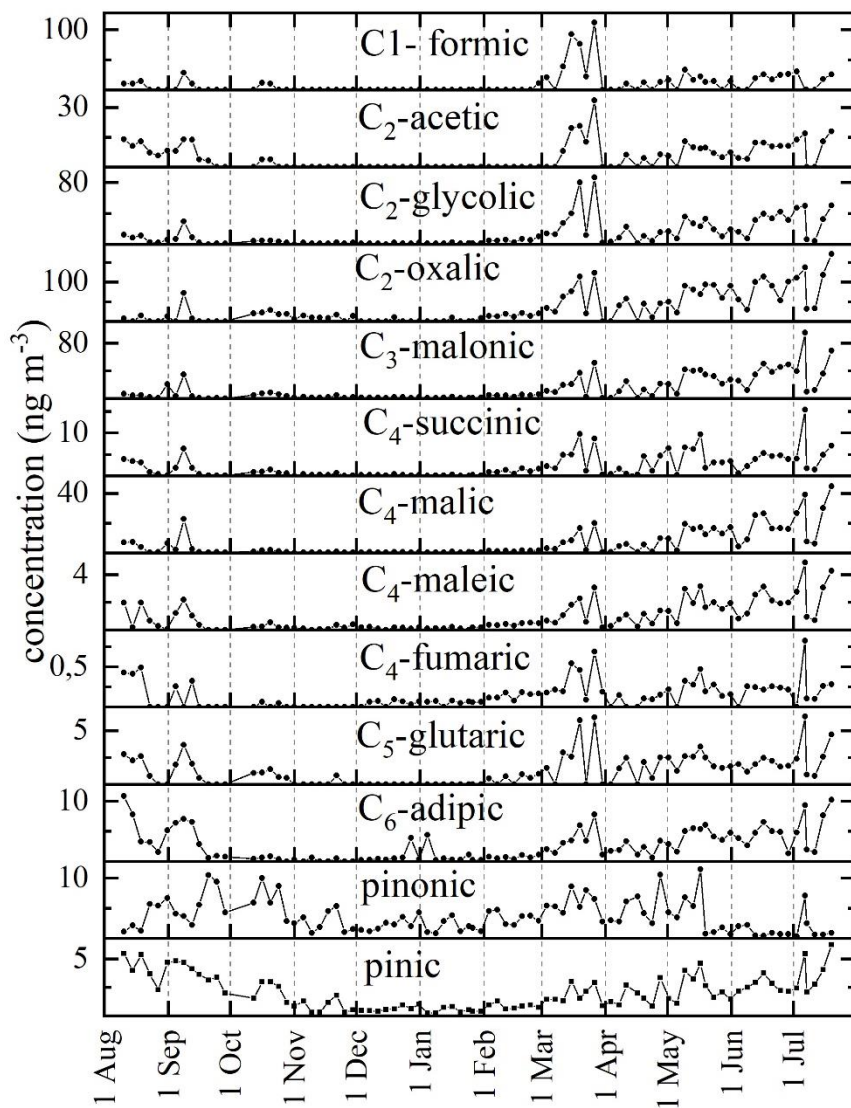


Figure S5. Annual trend of organic acids in the aerosol collected at MRG between August 2021 and July 2022

## Complete description of elemental composition and possible tracer of aerosol sources

The use of trace element enrichment factors (EFs) is useful to highlight the contribution of non-natural or anthropogenic sources on elemental concentrations. An EF is calculated as follows:

$$EF_i = (i/j)_{\text{atmosphere}} / (i/j)_{\text{upper crust}}$$

where  $EF_i$  is the enrichment factor of element  $i$ ,  $j$  is a reference element of crustal origin,  $(i/j)_{\text{atmosphere}}$  is the ratio of element  $i$  to element  $j$  in the atmosphere and  $(i/j)_{\text{upper crust}}$  is the ratio of element  $i$  to element  $j$  in the upper crust (Wedepohl, 1995). We used Al as the reference element in our EF calculations following the suggestion of Gao et al. (1992). A crustal derived element (geogenic) shows an EF near 1, while significantly higher EF values indicate a non-geogenic (not crustal-derived) element: EF between 10 and 100 indicates a moderate enrichment while an EF above 100 indicates a prevalent not-crustal origin.

Similarly, we can calculate the marine enrichment factors (MEFs) relative to sea water concentrations (abundance in sea water from Nozaki, 2010) to highlight a possible marine source. MEFs were calculated as:

$$MEF_i = (i/j)_{\text{atmosphere}} / (i/j)_{\text{sea water}}$$

ssCa, sea salt derived Ca (calculated as  $[Ca] - (0.038 * [Na])$ ) was used as reference element ( $j$ ) of marine origin. A MEF  $< 1$  indicates a marine derived element, while higher values indicate a moderate enrichment (10-100) and high values ( $> 100$ ) relative to sea water, exclude the prevalence of marine sources.

On the basis of the EF values (Fig. S6a), we can hypothesize that the prevalent source for K, Na, Cs, Sr, Ti, Ca, V, Ba, Li, Mn, Rb, Co, Tl, Fe, Mg and Light Rare Earth Elements (LREE) is geogenic with some exceptions during fall and winter seasons when a moderate enrichment of these elements is evident. Medium Rare Earth Elements (MREE), Heavy Rare Earth Elements (HREE), and U show a high variability between geogenic and non-geogenic sources especially from fall 2021 to spring 2022. Cr, Cu, Pb, Zn, Ni, Sb and Cd show a prevalently non geogenic source during all the seasons, but not exclusively, especially during the two summer periods and the winter one. Ag and Mo show always a clear non geogenic source. The MEF values (Fig. S6b) allow us to see that Na, K, Sr, Mg, Ca, are partially related to a marine source. All other elements show a value higher than 1 indicating a prevalently non- marine source.

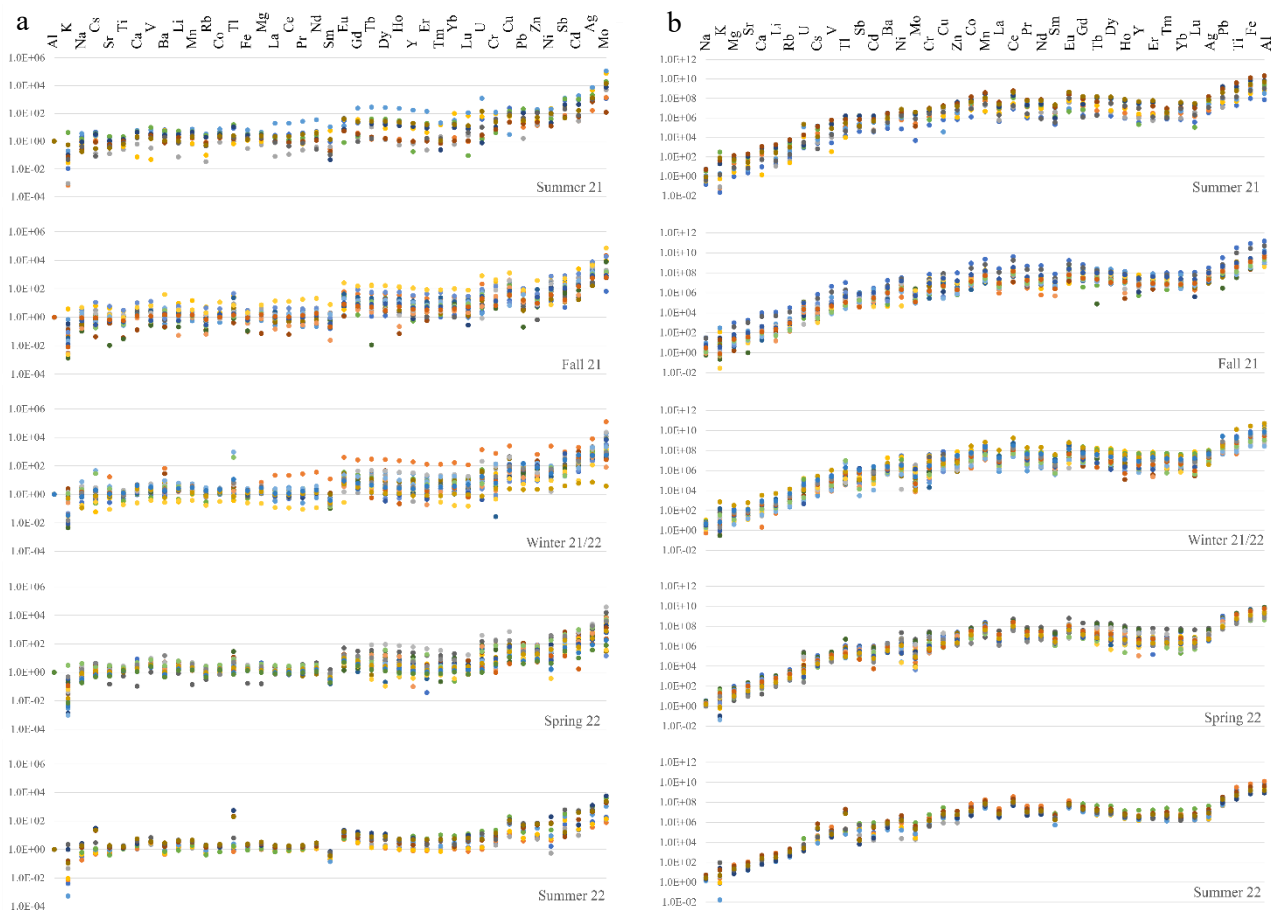


**Figure S6. (a) EFs: enrichment factors calculated using Al as reference element. (b) MEFs: marine enrichment factors calculated using ssCa as reference element.**

To better discriminate between the possible sources, we evaluated various elements by considering their ability to characterize certain sources. The principal sources of MRG aerosol are a local crustal contribution, long range transport of Saharan dust, sea-salt spray from the Mediterranean basin, biomass combustion, either from fires or from domestic heating, and to a lesser extent, traffic, refinery emissions, and oil combustion processes.

To do a first survey of sources other than crustal ones that could characterize the MRG samples, we plotted a ternary diagram of La-Ce-Sm (Fig. S7), three rare earth elements that show a clear geogenic origin based on their EF values. Using this method, all seasons show different sources other than the earth's crust, although it is possible to recognize a prevalently crustal origin in the fall and winter samples, even if not exclusively so. In the spring and summer samples sources are prevalently different to the crust.

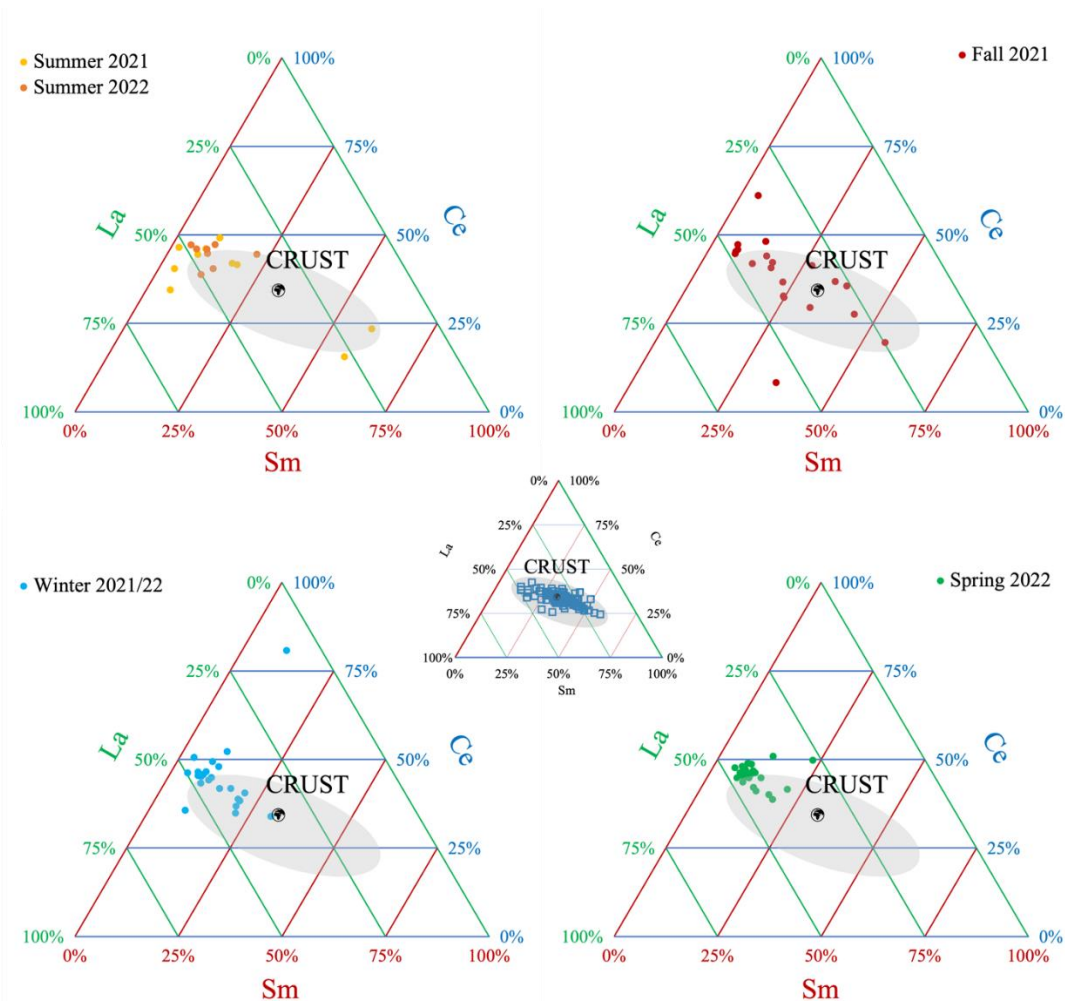


**Figure S7.** Ternary diagrams La-Ce-Sm. La and Sm were multiplied by 2 and 10 respectively to have the upper continental crust composition at the center of the graph. The grey ellipse represents the crustal composition of the area around MRG station (data from Lustrino et al. 2019 and references therein).

Due to the high elevation of MRG station, we firstly considered possible origins from natural sources after both local and long-range transport. EF factors (Fig. S6) indicate some elements as having prevalent, but not exclusively, geogenic origins. In particular, we have focused our attention on the Mg distribution, whose source could either be the crust and/or sea-salt spray. The comparison between the water-soluble fraction and the total content of Mg reveals the two possible origins of this element. In the Fig. 7a we compare the distribution of water-soluble Mg ( $Mg^{2+}$ , light green line) and total Mg (Mg, green line) normalised to the mass of  $PM_{10}$  collected. Mg of a geogenic (crustal) origin is expected to be mostly non-water soluble while Mg from sea-salt spray is mainly related to the water-soluble fraction. Due to the different concentrations, the peaks of  $Mg^{2+}$  in Fig. 7a are not very evident, the same data are reported in Fig. 8b and c where the scale differences make the variances in the signal more obvious.

In Fig. S8a and S8b various Mg peaks of both the soluble and total fractions, can be recognized. During fall 2021 some peaks of  $Mg^{2+}$  and Mg are evident, while in late winter a peak of total Mg is visible in correspondence with the Saharan Dust event, but the corresponding  $Mg^{2+}$  value is very low. Considering that Mg is one of the major components of sea-salt spray and is also present at very high levels in Saharan dust we can use the Mg fractions as specific tracers, in Mediterranean region, of these two different sources.

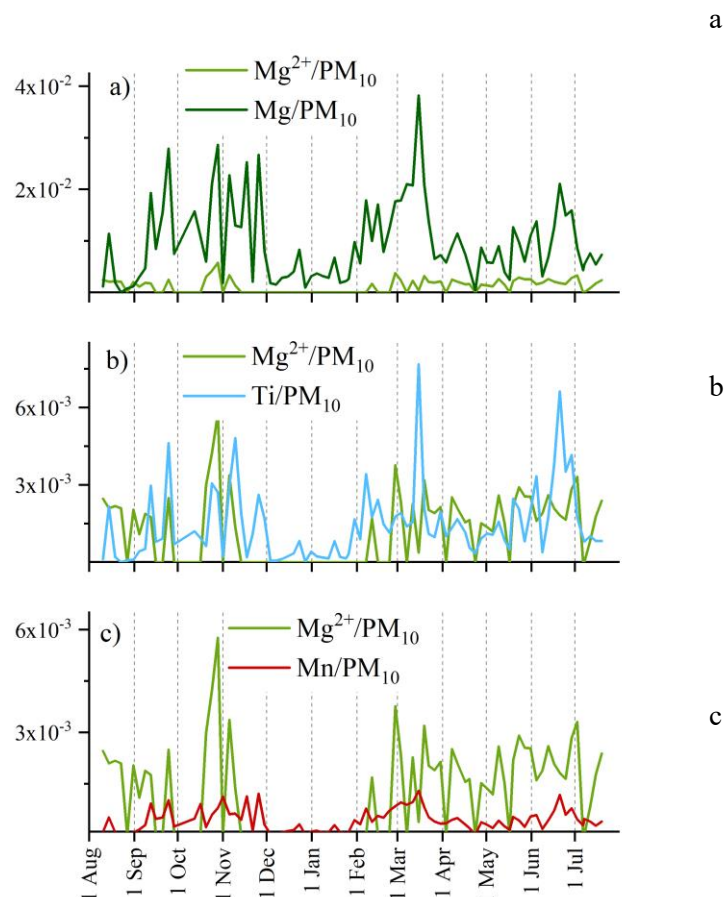


**Figure S8. Comparison between water soluble fraction of Mg and total fraction of Mg (a), total Ti (b), total Mn (c). Mg, Ti and Mn are normalized using PM<sub>10</sub> mass concentration.**

Mg from sea salt origin, has in fact, a high solubility while Mg from Saharan dusts, originating from clay minerals, has a low solubility (Perrino et al., 2008). Based on this, we can attribute the Fall 2021 peaks to a marine origin while the late-winter peak seems to be related to a Saharan event, also considering that during Saharan events there is a high dust loading (Fig. 1). In Fig. S8 b and c the distribution of total Ti and total Mn, respectively, are compared with the water-soluble fraction of Mg to try and determine the possible source of the late-winter PM<sub>10</sub> peak. Ti and Mn are recognized as indicators of Saharan dust (Perrino et al., 2008); the observed distributions in Fig. 7b and c confirm the evidence of the Saharan input, already highlighted by the Mg distribution.

In Fig. S9, Ti, Mn and Mo, a third element related to the North African area (Wong et al., 2020a), are plotted highlighting samples that could be completely or, at least, partially related to a North African source. Only one sample can be recognized as fully related to a Saharan event, the spring one (blue dot in Fig. S9). Also, two other spring samples (green dots) could also be partially related to possible minor events characterized by a North African component or by a component coming from the route followed by Saharan dusts passing through Spain and France before reaching the Italian Alps.

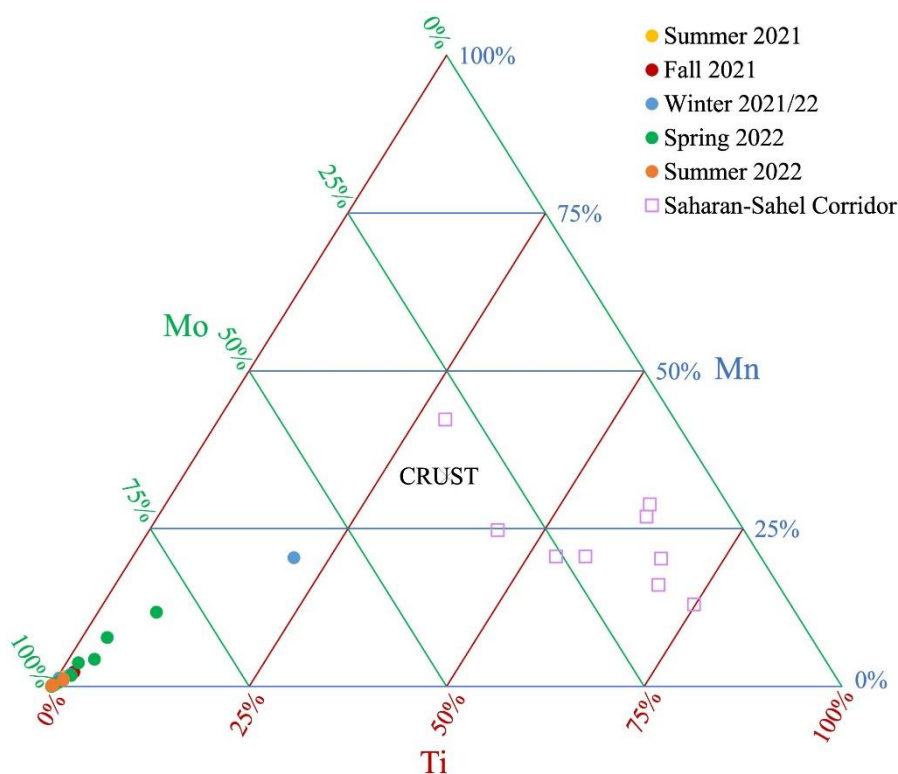


**Figure S9. Ternary diagrams: Mo-Mn-Ti. Ti and Mn were multiplied by 0.00045 and 0.00265 respectively to have the upper continental crust composition at the center of the graph. Data of Saharan-Sahel Corridors from Moreno et al (2006).**

Other sources to be considered when characterizing aerosol samples are for example, biomass burning, both from fire and domestic uses. To highlight the possible contribution of this kind of source to the MRG aerosol composition, we plotted three rare earth elements Eu-Ho-Yb in a ternary diagram (Fig. S10). These elements give information on fire events, and can distinguish between different biomass ashes: in particular, it is possible to discriminate hardwood and softwood fires from grass and shrub fires (Dukes et al., 2018). In Fig. S10 we show the sample distributions; in comparison with literature data for tree and biomass ashes as reported in (Flood, 2019; Perämäki et al., 2019; Vassilev and Vassileva, 2020).

The fall samples, red dots, and some spring samples, green dots, are in the tree ash region, indicating hardwood and softwood burning as a possible source for PM, probably coming from domestic heating with wood (and coal), that it is known to producing this type of signal in aerosol. Some samples are in the shrub area and in the region between bare ground and shrub (Dukes et al., 2018). In the spring and summer of 2022 there were high temperatures, severe droughts, and many fires, especially in Spain. So, the samples in the area between bare ground and shrubs, in Fig. S10, may be linked to these wildfire events. In particular, the spring samples, the green dots, in this region are the same samples that were already highlighted in Fig. S10 and hypothesized as related to minor Saharan events or to the Spain-France region. On this basis of these results, the samples can be linked to fire events instead of Saharan events.

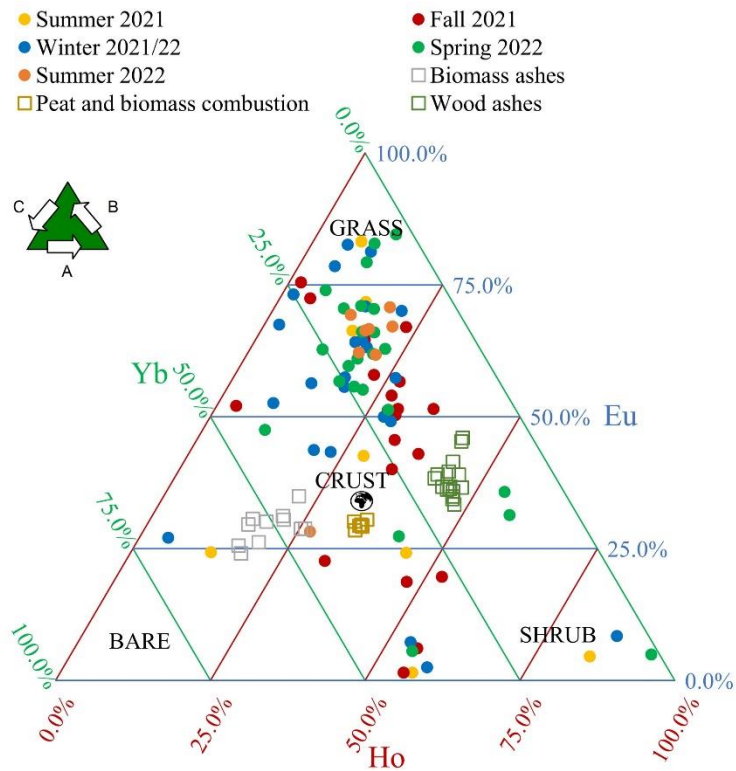


**Figure S10. Ternary diagram of Eu-Ho-Yb. Eu and Yb were multiplied by 0.64 and 0.41 respectively to have the upper continental crust composition at the centre of the graph.**

We plotted the MRG aerosol samples in a ternary diagram based on V, La and Ce with the aim of recognizing aerosol from three possible anthropogenic sources related to refinery emissions, oil combustion processes and vehicular traffic emissions (Fig. S11).

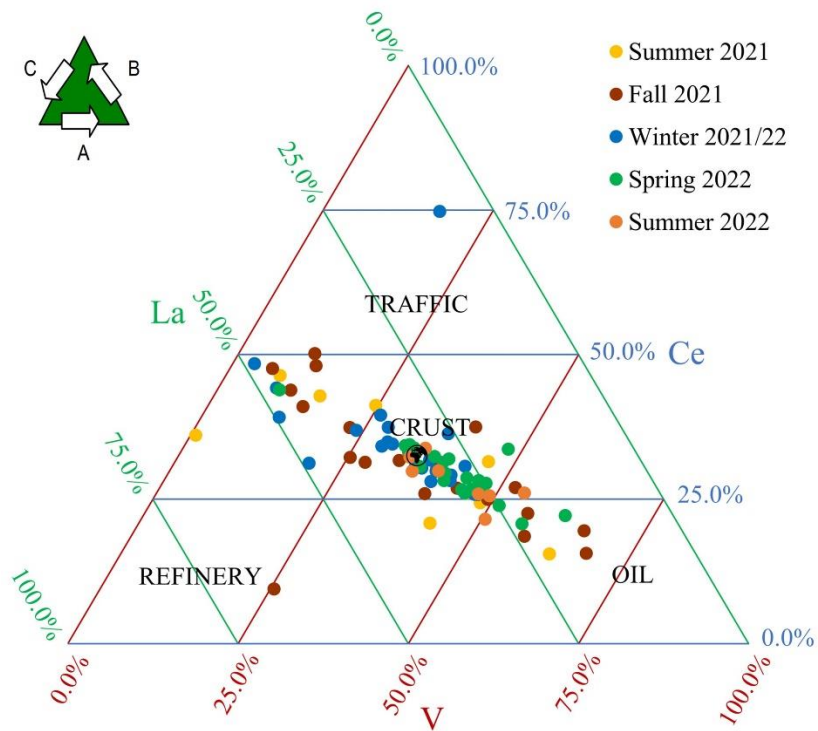


**Figure S11. V-La-Ce ternary graph. La and Ce were multiplied by 3.1 and 1.54 respectively to have the upper continental crust composition at the center of the graph. Indication of oil, traffic, and refinery corners from (Moreno et al., 2008).**

Samples are mainly distributed in the central part of the diagram, around the crustal composition, indicating a prevalently crustal source for V. It is also possible to see, however, a group of samples shifting toward higher values of Ce and La and another group toward higher values of V. These two different groups, seem to indicate possibly different anthropogenic sources: namely traffic/refinery and oil combustion processes respectively.

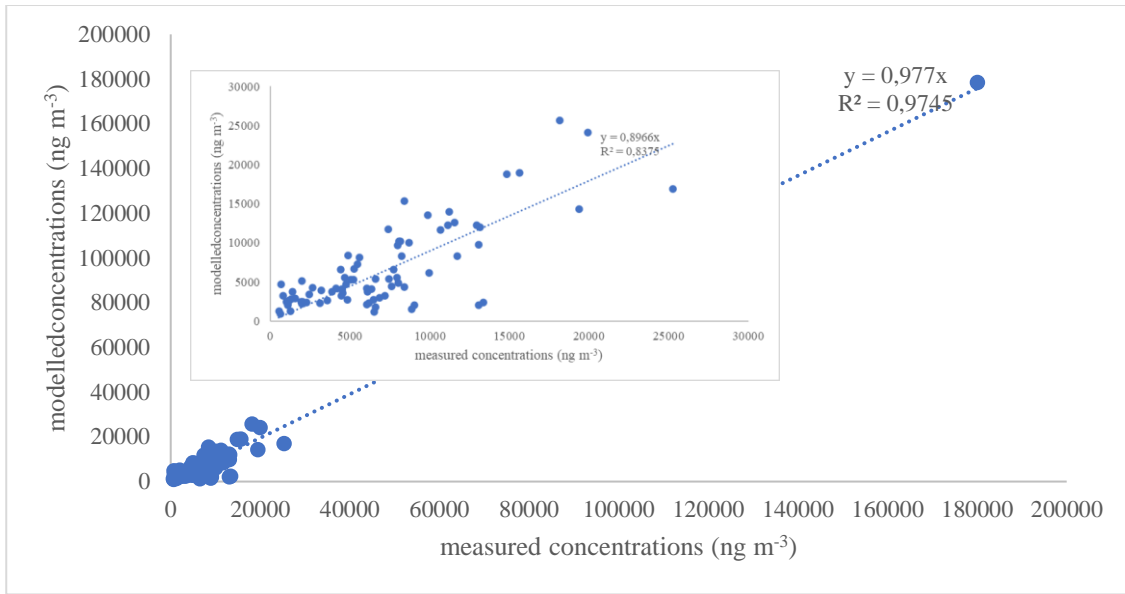
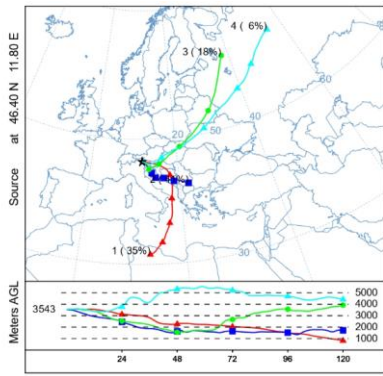
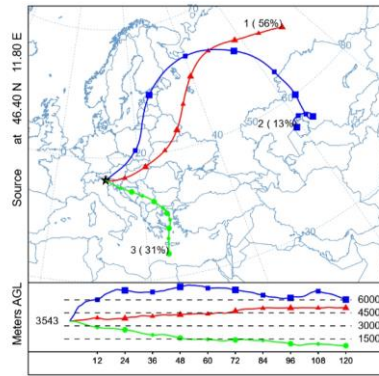


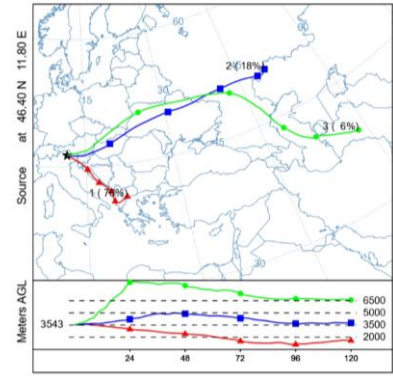
**Figure S12.** Comparison between measured and modelled concentrations obtained with PMF approach. In the box inside, the outlier point of Saharan Dust was excluded to evaluate the quality of reconstruction without the artifact due to the outlier point.



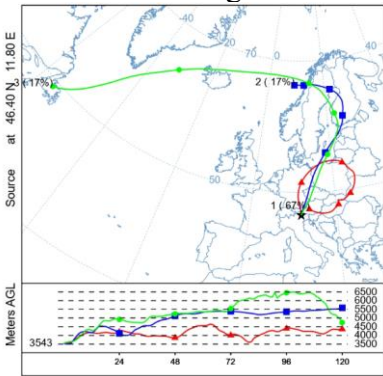
10-14 August



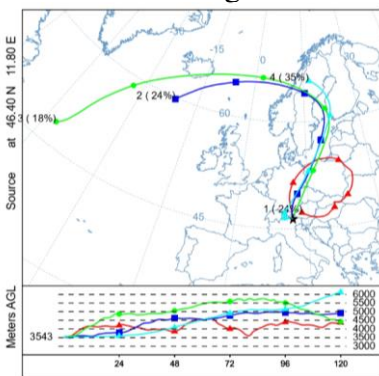
14-18 August



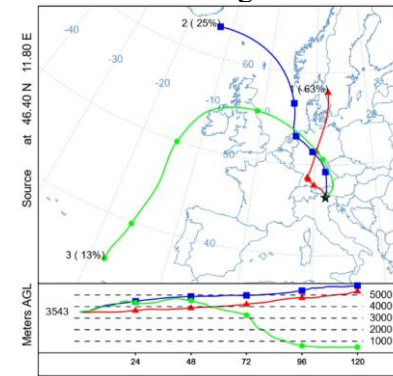
18-22 August



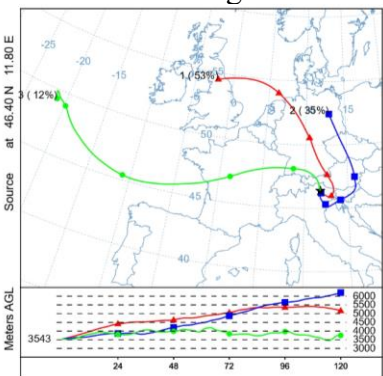
27-31 August



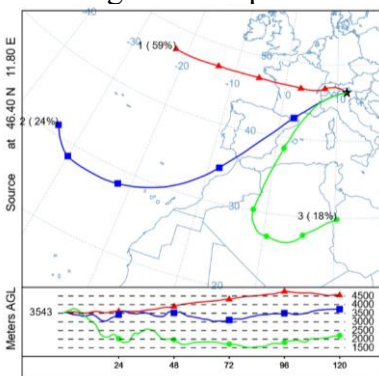
31 August - 4 September



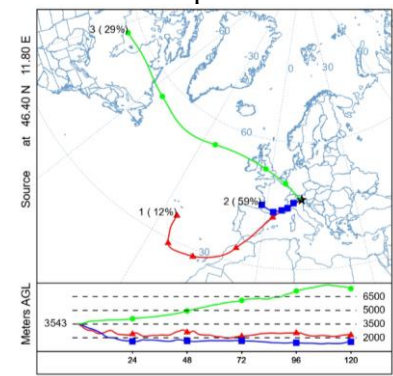
4-8 September



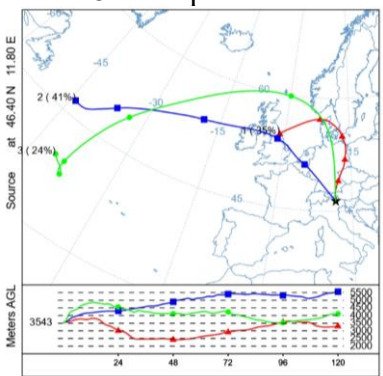
8-12 September



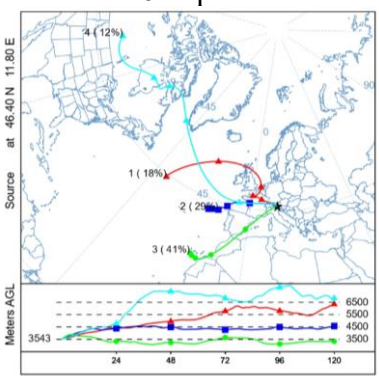
12-16 September



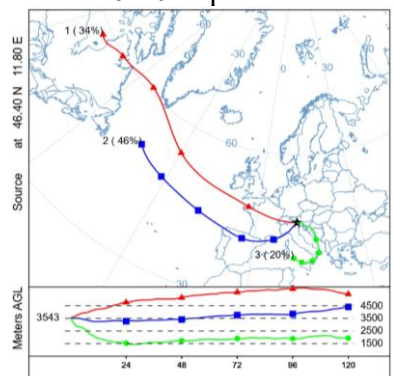
16-20 September



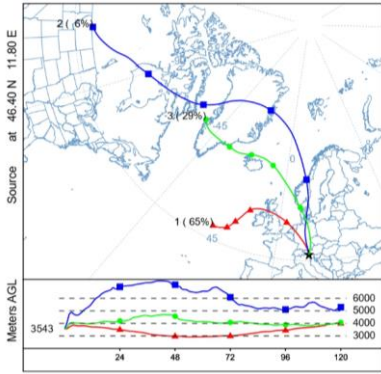
20-24 September



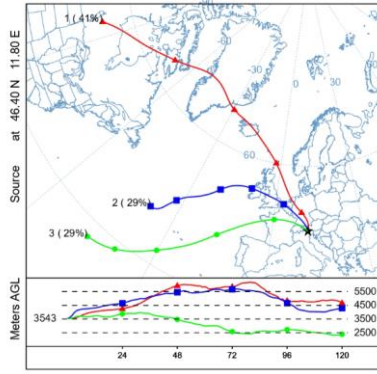
24-28 September



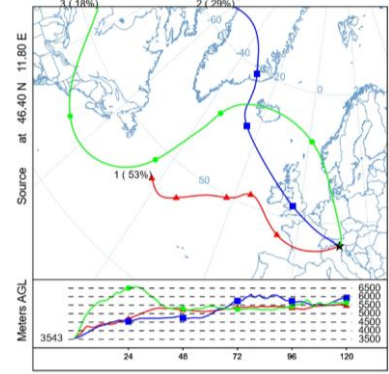
28 September - 10 October



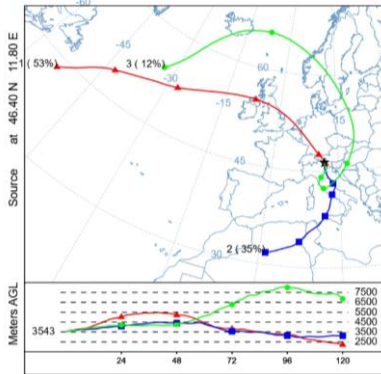
12-16 October



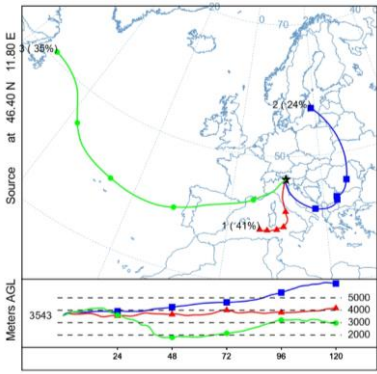
16-20 October



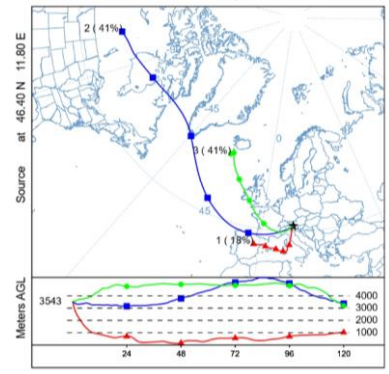
20-24 October



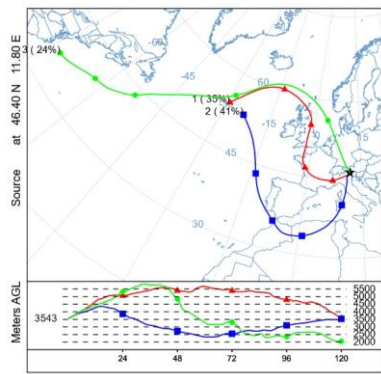
24-28 October



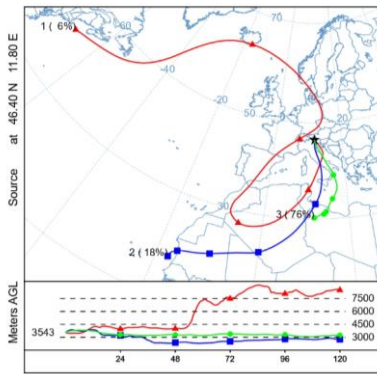
28 October - 1 November



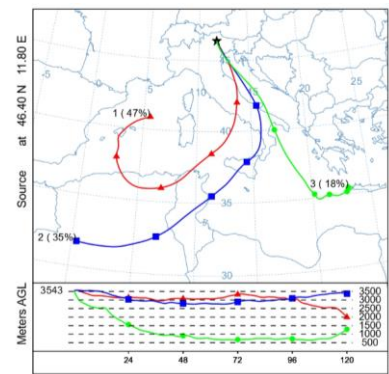
1-5 November



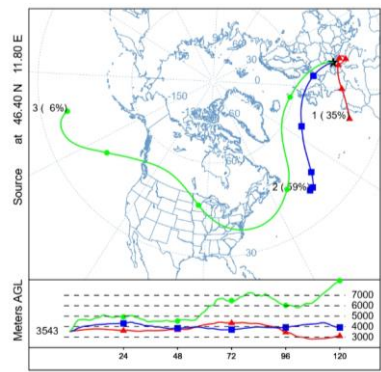
5-9 November



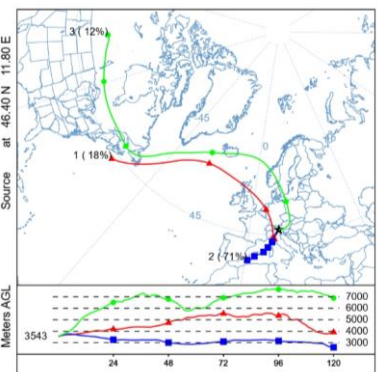
9-13 November



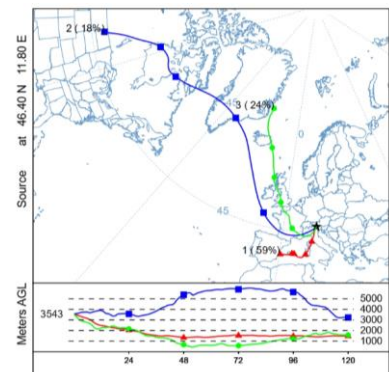
13-17 November



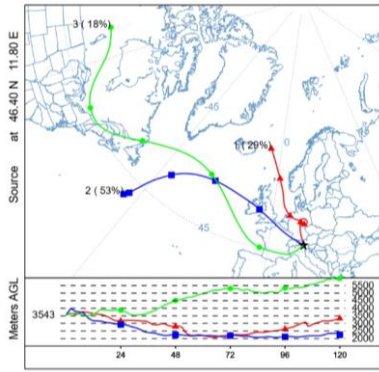
17-21 November



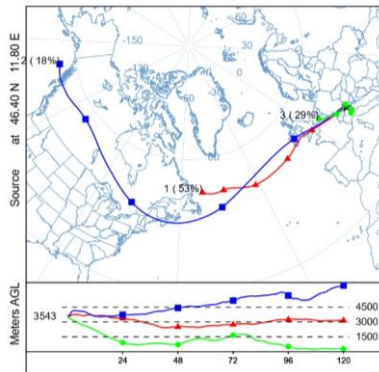
21-25 November



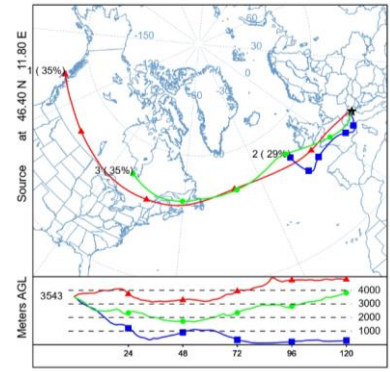
25-29 November



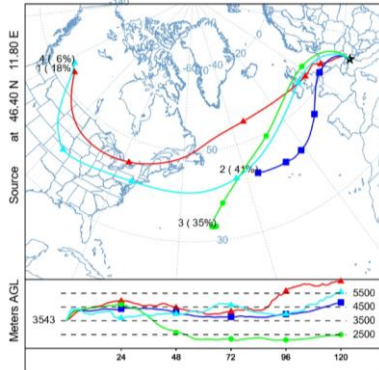
29 November – 3 December



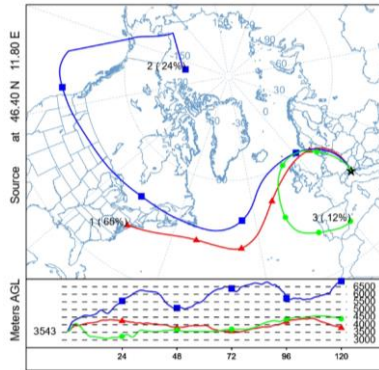
3-7 December



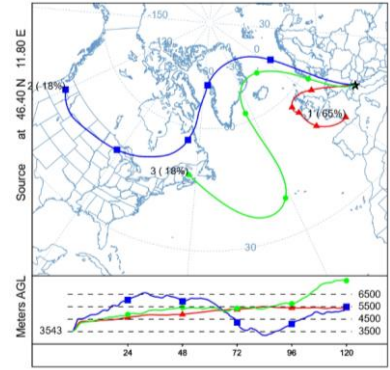
7-11 December



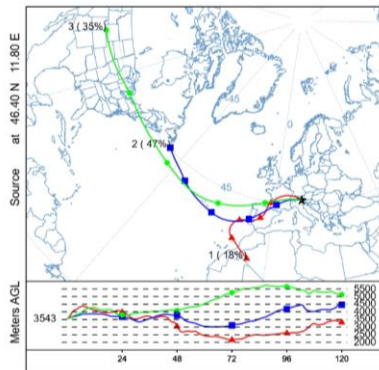
11-15 December



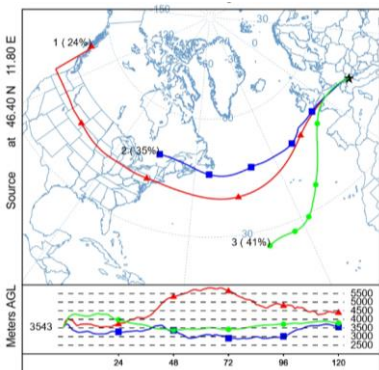
15-19 December



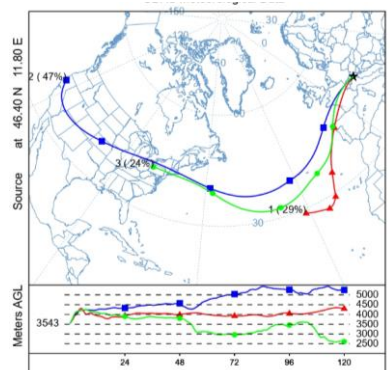
19-23 December



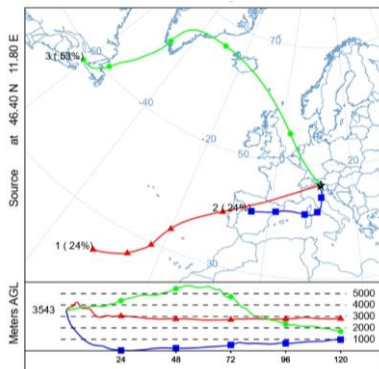
23-27 December



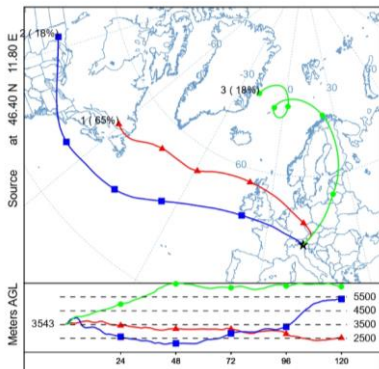
27-31 December



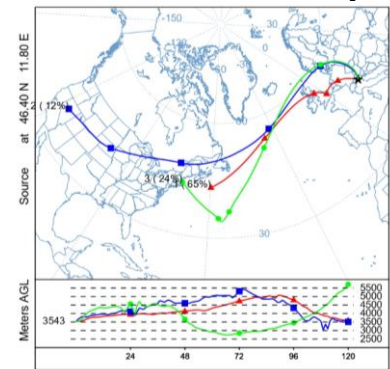
31 December – 4 January



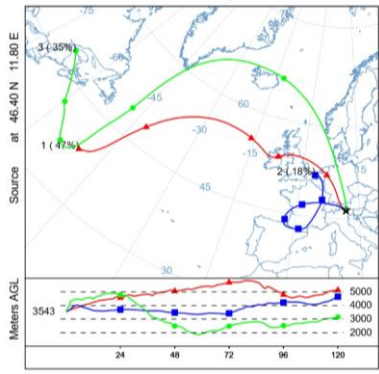
4-8 January



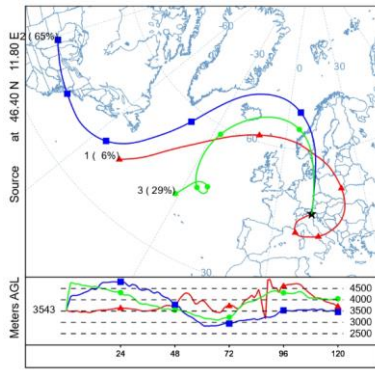
8-12 January



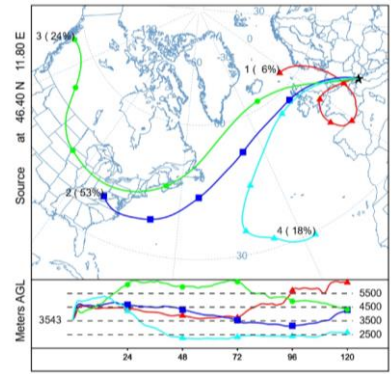
12-16 January



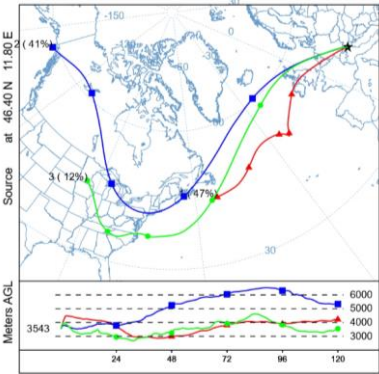
16-20 January



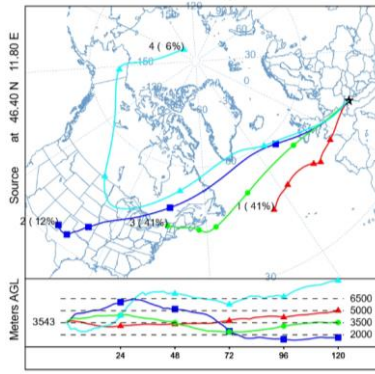
20-24 January



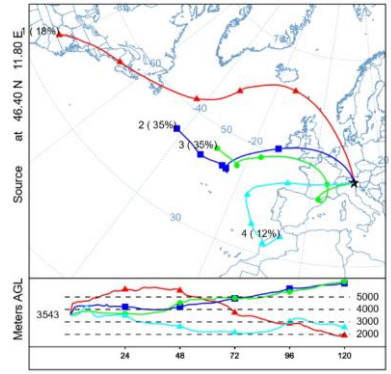
26-30 January



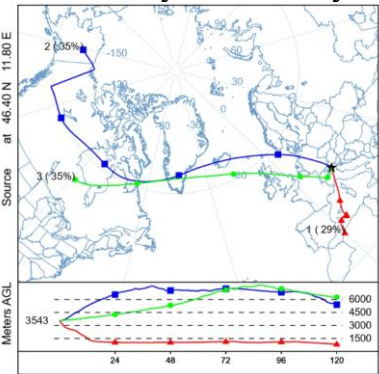
30 January - 3 February



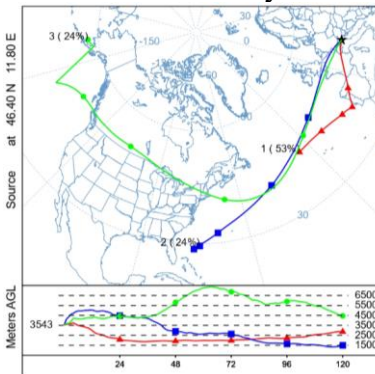
3-7 February



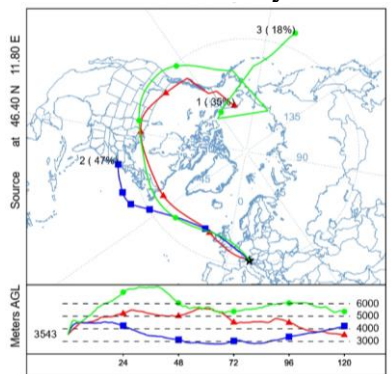
7-11 February



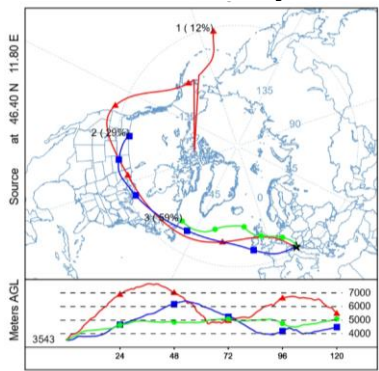
11-15 February



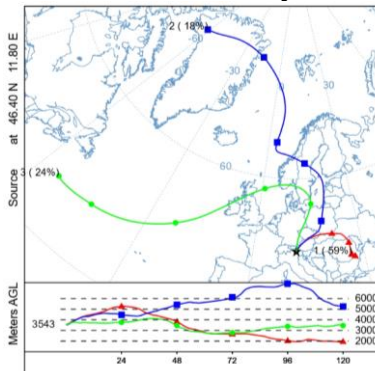
15-19 February



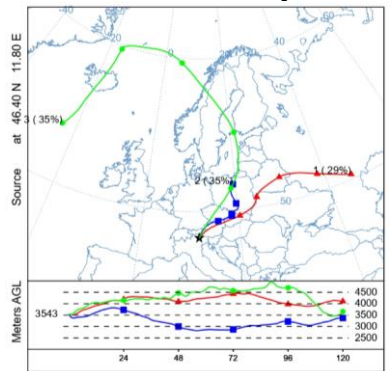
19-23 February



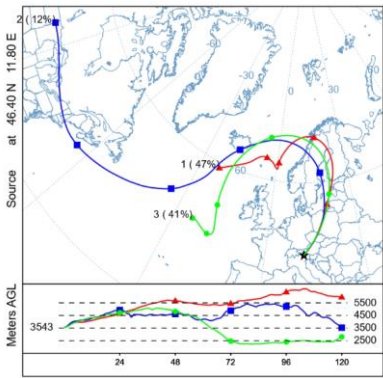
23-27 February



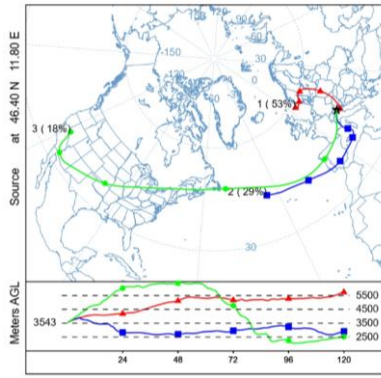
27 February - 3 March



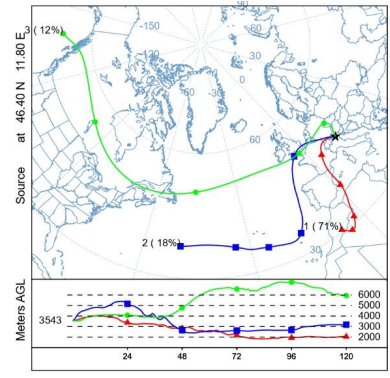
3-7 March



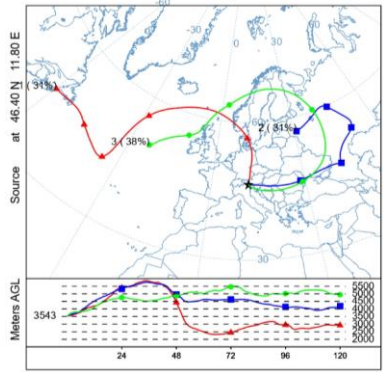
7-11 March



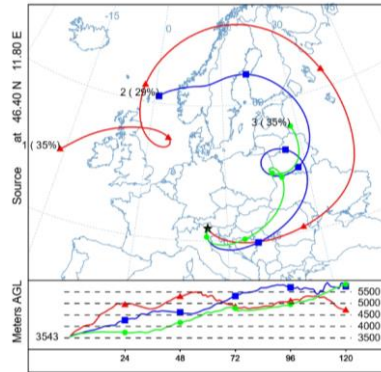
11-15 March



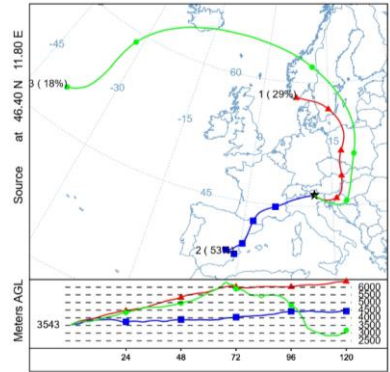
15-19 March



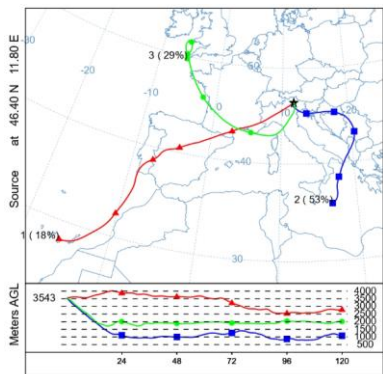
19-22 March



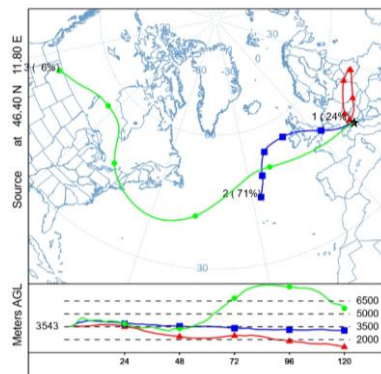
22-26 March



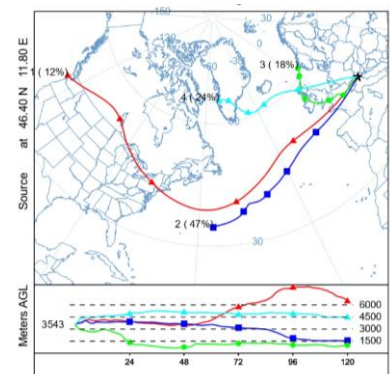
26-30 March



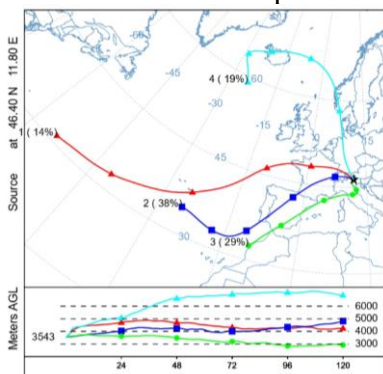
30 March - 3 April



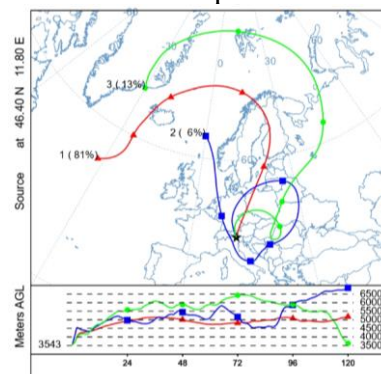
3-7 April



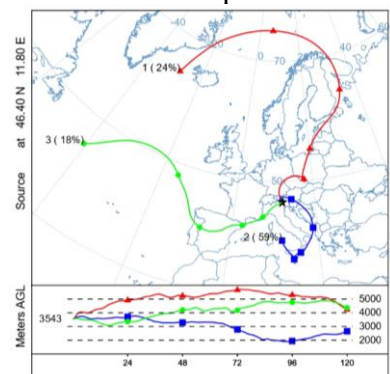
7-11 April



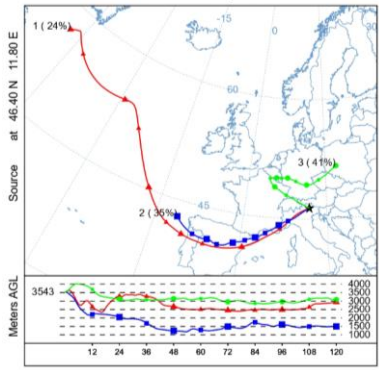
11-16 April



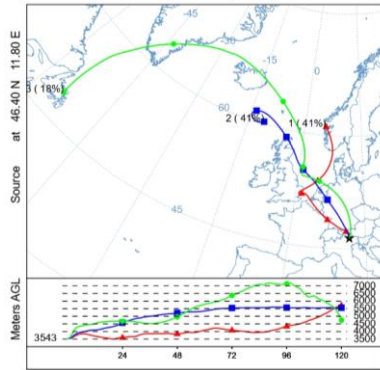
16-19 April



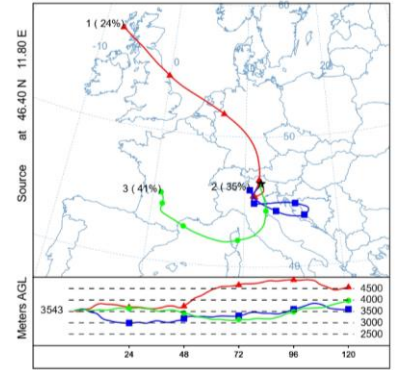
19-23 April



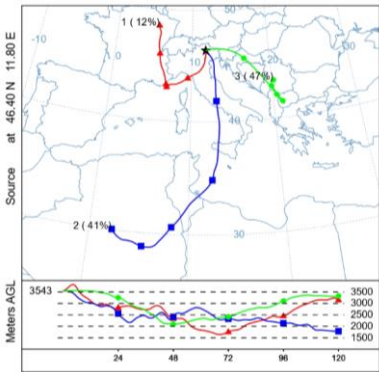
23-27 April



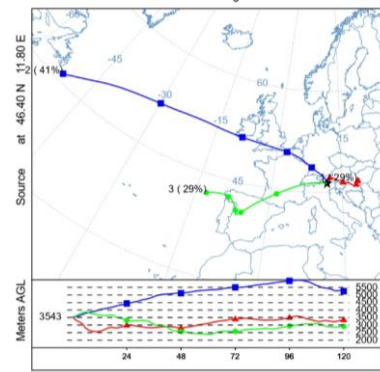
27 April – 1 May



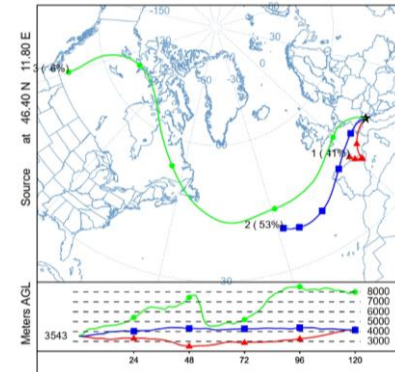
1-5 May



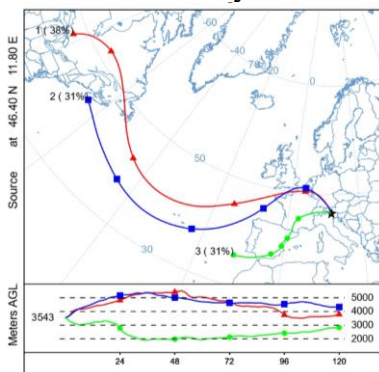
5-9 May



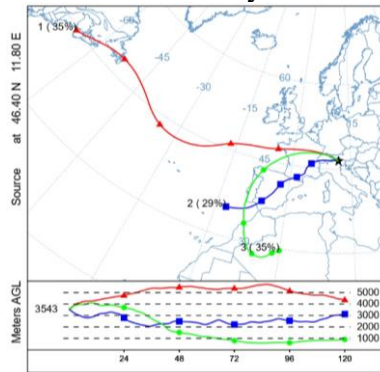
9-13 May



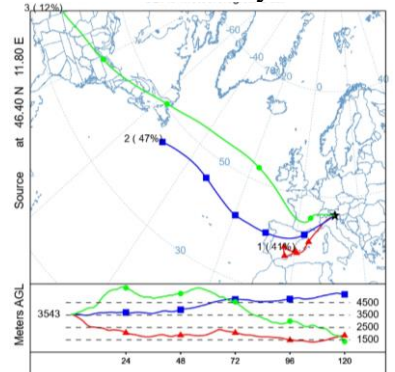
13-17 May



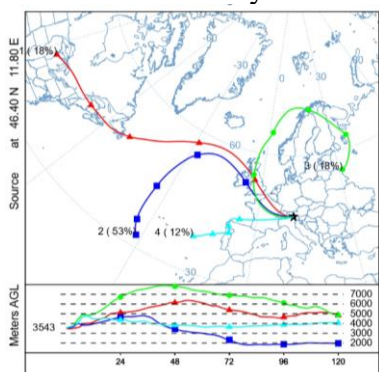
17-19 May



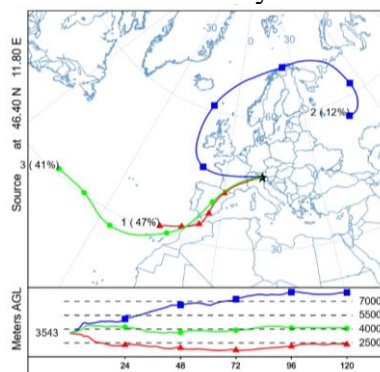
19-23 May



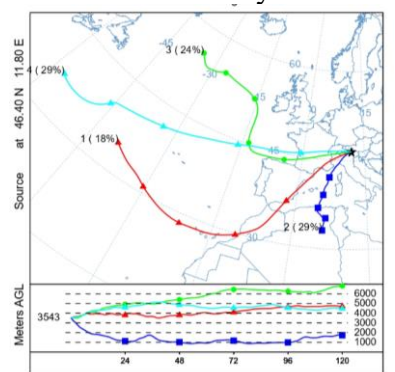
23-27 May



27-31 May



31 May – 4 June



4-8 June

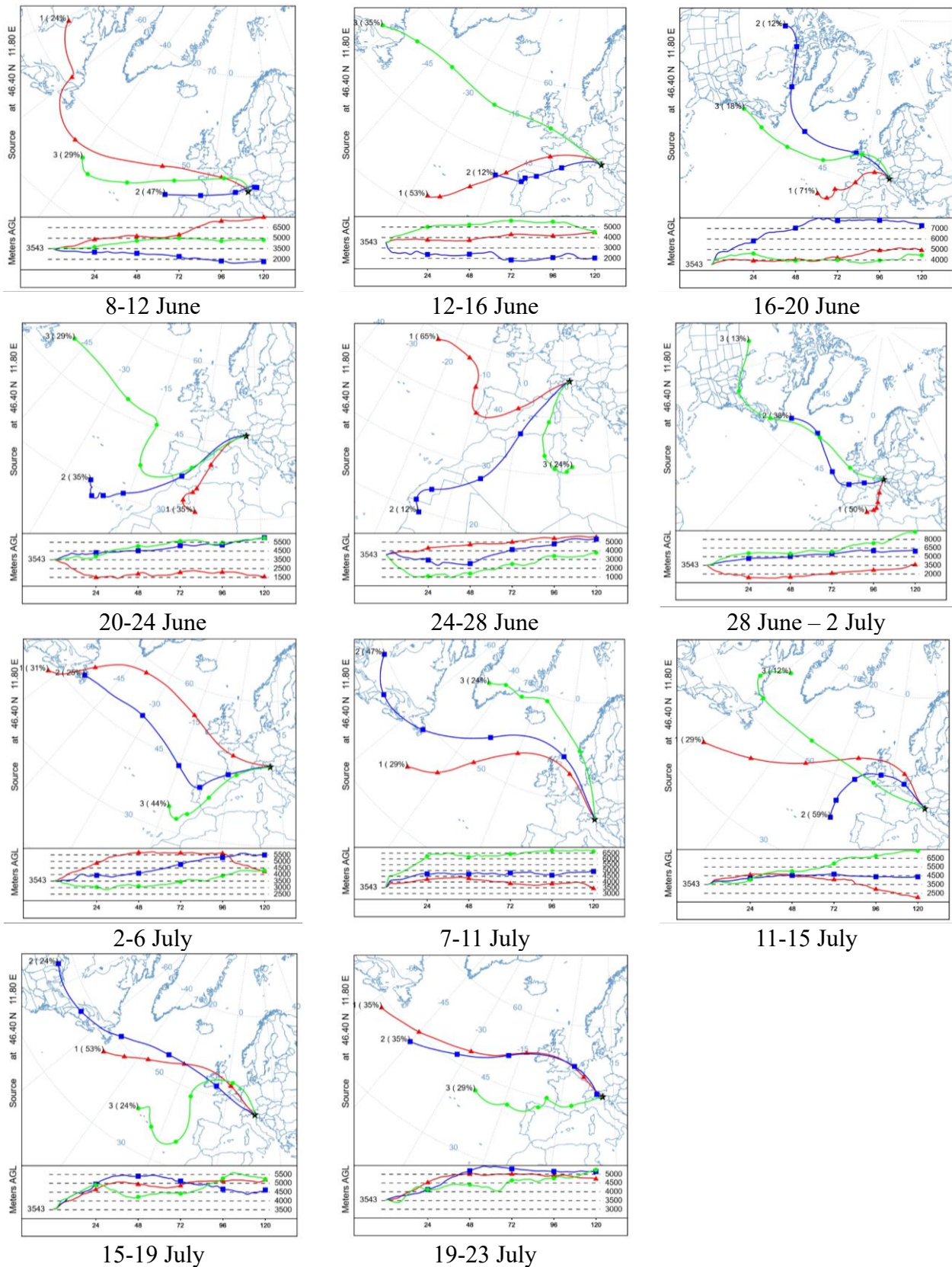


Figure S13. 5-days back-trajectories of air masses calculated for each sample. The starting point is considered the elevation of Col Margherita Station plus 1000 m in to avoid the surrounding orography.

Table S1. Linearity of each species plotted the observed data with the modelled ones.

Species	Intercept	Slope	R <sup>2</sup>
PM <sub>10</sub>	533.497	0.757	0.961
Na <sup>+</sup>	-3.036	0.802	0.440
Na	-40.600	1.666	0.921
NH <sub>4</sub> <sup>+</sup>	42.962	0.502	0.700
K <sup>+</sup>	1.018	0.688	0.615
Mg <sup>2+</sup>	-2.301	1.095	0.566
Mg	31.087	0.480	0.984
Ca <sup>2+</sup>	-13.345	0.838	0.854
Cl <sup>-</sup>	2.757	0.386	0.780
NO <sub>3</sub> <sup>-</sup>	65.848	0.179	0.290
SO <sub>4</sub> <sup>2-</sup>	116.850	0.538	0.508
MSA <sup>-</sup>	0.315	0.852	0.845
Br <sup>-</sup>	0.370	0.511	0.446
CA	11.724	0.373	0.596
D-FAA	0.148	0.501	0.655
L-FAA	0.368	0.647	0.594
PC	0.086	0.053	0.171
PDαP	2.571	0.201	0.073
Levoglucozan	0.703	0.082	0.290
Mannitol	0.137	0.430	0.505
Glucose	0.263	0.459	0.560
Ti	4.832	0.347	0.988
Mn	0.938	0.624	0.992
Mo	1.670	0.076	0.054
Cu	-1.991	1.648	0.388
Pb	-0.287	1.018	0.581
V	0.125	0.477	0.992
U	0.012	0.398	0.425
Ag	0.047	-0.011	0.004
Sb	0.018	0.151	0.299
Fe	56.711	0.407	0.989
La	0.042	0.460	0.990
Ce	0.087	0.448	0.989
Sm	0.007	0.597	0.991
Eu	0.002	0.443	0.983
Ho	-0.0003	0.662	0.951
Yb	0.003	0.462	0.971